IET Renewable Power Generation

*Research Article*

IET Journals
The Institution of Engineering and Technology

# Control and operation of a three-phase local energy router for prosumers in a smart community

ISSN 1752-1416
Received on 16th May 2019
Revised 20th August 2019
Accepted on 17th December 2019
E-First on 25th February 2020
doi: 10.1049/iet-rpg.2019.0589
www.ietdl.org

*Carlos Roncero-Clemente[1], Nuno Vilhena[2], Vasco Delgado-Gomes[2] ✉, Enrique Romero-Cadaval[1], João F. Martins[2]*

[1]*Power Electrical and Electronics System Research Group, University of Extremadura, 06006 Badajoz, Spain*
[2]*Faculty of Sciences and Technology, NOVA University of Lisbon, CTS-UNINOVA, 2829-516 Caparica, Portugal*
✉ *E-mail: vmdg@uninova.pt*

**Abstract:** From the electrical energy point of view, the smart community (SC) concept is meant to be as a sustainable and environmentally friendly alternative to the classical configuration. The SC includes small-scale renewable energy sources (RES) and small-scale energy storage system (ESS). The SC energy management system acts as an aggregator, aiming to assure benefits for community stakeholders. These trends led to the energy routers (ERs) concept. This study proposes and describes the control strategies for these ERs to contribute to the SC goals. The approach of these strategies increases the RES adjustability, contributing to maintain the ESS state of health. The ER is able to operate simultaneously with active and reactive power control, besides compensating SC grid voltage imbalances, and providing ancillary services to the SC. The proposed control strategies are validated by simulations and experiments.

## 1 Introduction

The concept of the smart grid (SG) was defined as:

> '*advanced power grid for the 21st century include the addition and integration of many varieties of digital computing and communication technologies and services with the power-delivery infrastructure. Bidirectional flows of energy and two-way communication and control capabilities will enable an array of new functionalities and applications that go well beyond 'smart' meters for homes and businesses'* [1].

The idea mainly arose from the challenge of integrating distributed renewable energy sources (RES) in order to reduce greenhouse emissions and energy losses [2]. This integration increased the issues related to the inherent intermittency of RES, e.g. poor energy management [3]. Concurrently, the focus was on the energy storage system (ESS) research and its application. The coupling between RES and ESS provides a smoother injected power by RES, load peak saving, effective spinning reserve, better matching between the consumption and generation, besides the avoidance of transporting energy in excess, and facilitating the distribution grid operation [4–8].

A modern concept is the so-called smart communities (SCs), which takes advantage of the SG knowledge, allowing effective demand-side management [9]. The SC can be defined as a distributed system consisting of a set of smart homes, RES and ESS which utilise SC controllers (e.g. genetic algorithms and game-theoretic models) to enable smart power management within the SC [10]. It requires power electronic converters with general purposes (both in DC and AC), small-scale ESS (known as micro ESS) shared by several homes in a community or not, integrated with small-scale RES installed at the residential level, advance metering infrastructure [11], and an optimal use of the information and communication technology [2]. In this sense, the trend goes towards the concept of energy routers (ERs) [4]. The use of the ER in the SC allows the consumer to obtain energy bills savings, as the electrical energy is provided by ESS, or by the RES (if the time-period of consumption matches that the production from renewables) [12]. Profits for owners of ESS or RES also appear, since they can sell the energy locally into the SC or to the market during high-price time periods [13]. This concept is meant to be as a sustainable and environmentally friendly alternative to the classical electric scenario. In this situation, the energy users become prosumers, defined as SC users that combine energy production and consumption [14]. However, the electrical system is still today a mix of centralised and small-scale smart distributed systems. Fig. 1 shows a possible configuration of an SC comprising several prosumers [15]. Each prosumer has an ER to act as an interface between their distributed energy resources and the SC point of common coupling (SC-PCC).

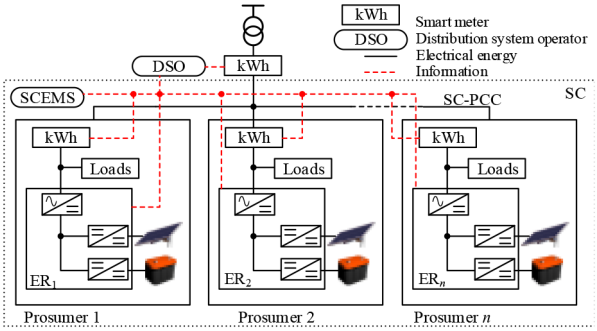


**Fig. 1** *Configuration of an SC*

ER control and supervision are carried out by the SC energy management system (SCEMS) [4]. It acts as an aggregator of resources and coordinated them to assure benefits for every community stakeholder [7]. The SCEMS receives and computes data from sensors and equipment installed in the SC such as ESS state of charge (SoC), weather forecast, energy prices, load profiles, RMS SC grid voltages and frequency at different buses, imbalance coefficients etc. Based on different optimisation algorithms or SC goals [14–21], the SCEMS defines the reference values to each local ER for both active and reactive power (Fig. 2). A coordinated strategy among prosumers based on the individual batteries' SoC demonstrates a significant reduction on the energy interchanged, and the charging/discharging schedule or set-point calculation is carried out by means of a genetic algorithm [14]. Photovoltaic (PV) prosumers are considered in an energy sharing model, taking into account the price-based demand response and the PV costs [16]. The PV prosumers decide the energy prices, in order to schedule their PV energy production and loads by means

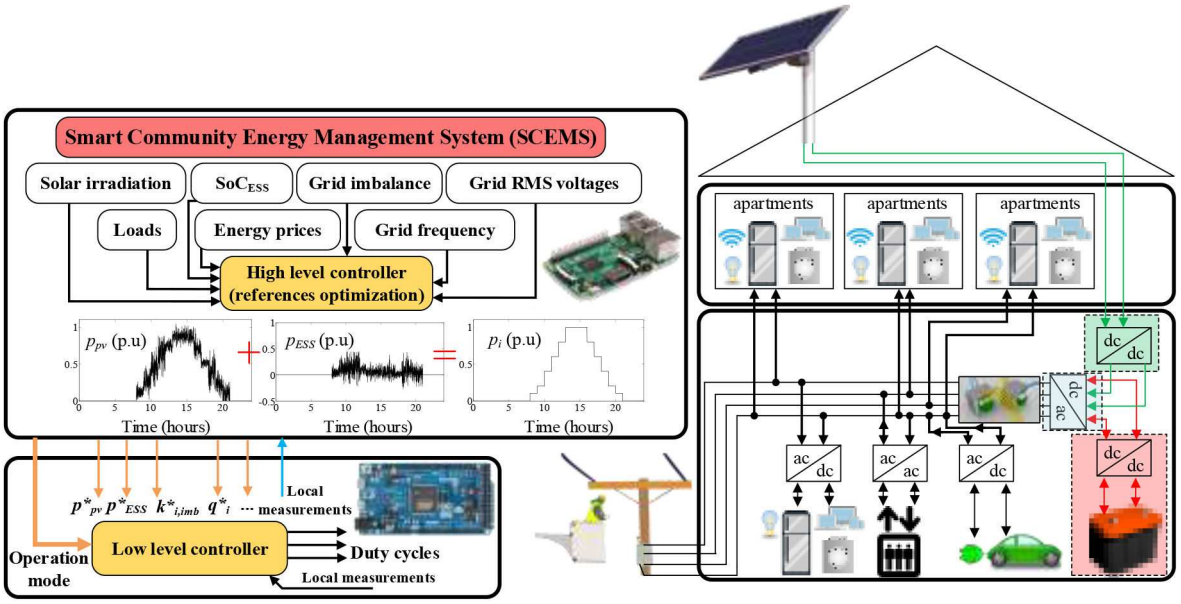


**Fig. 2** *General architecture of the ER and SCEMS, within a prosumer's house*

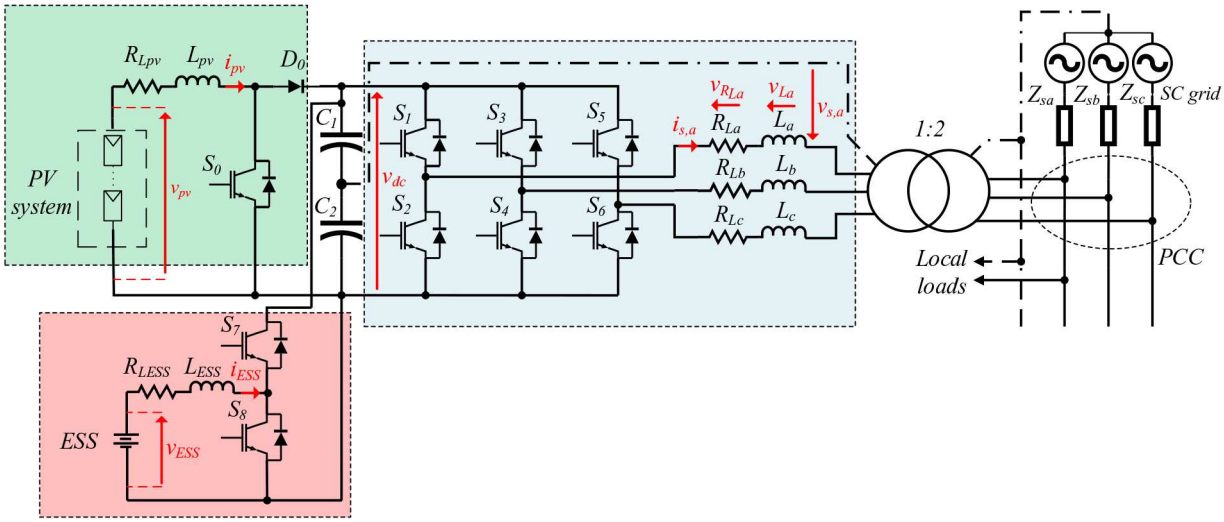


**Fig. 3** *Three-stages power topology of the developed ER*

of an iterative algorithm. Some clustering algorithms for virtually aggregate the prosumers enable an energy cost reduction [17]. A blockchain-based microgrid energy market to locally trade the distributed generation is studied in [18]. Some benefits, as the active local RES integration into the energy system are stated by this approach. A hierarchical decision-making strategy and a game-theoretic model were developed to manage the energy in [19] and in [15], respectively. In addition, the impact of the electric vehicles in an SC is also a very important issue to be considered [20]. Similar requirements and performance are requested to the SCEMS in case of multi-community systems [21].

Focusing the attention on the ER structure, a single-phase AC to AC configuration is presented, and predictive mode control for the second stage of the ER is also proposed, composed by a single-phase inverter [22]. A multi-port ER including medium and low voltage DC buses, a dedicated bus for the ESS and two AC ports (one to connect to the grid and the second supply AC load) as well as the different control strategies for each stage is studied in [23]. In this work, the grid-connection port is composed by a three-phase three-branches inverter, thus the unbalance compensation function cannot be performed. A similar multi-port topology has been also used, but experimental results are not provided [24].

This paper proposes and describes the implementation of control strategies and operation modes for the ER into an SC context, to accomplish the active and reactive power references coming from the SCEMS at the SC-PCC. The developed ER considers one RES (PV system) and one ESS but, both the control strategy and the topology may be extended for more RES or ESS resources. In this way, the ER provides ancillary services to the SC by controlling the active and reactive power flows [25], as well as compensating unbalance phases [26].

The paper is organised as follows: first, the ER topology is presented. Secondly, the control strategy to extract the references derived from the SCEMS set-points is explained in detail. Finally, the ER performance is demonstrated and validated by simulations and experimental results.

## 2 ER topology

The topology of the developed ER is displayed in Fig. 3. It consists of three power electronic converters sharing a common DC-link (capacitors $C_1$ and $C_2$). The aim of the used topology is to act as an active interface between the prosumer and the SC it belongs to.

A conventional DC–DC boost converter, composed of a filter inductor ($L_{pv}$), a single switch ($S_0$) and diode ($D_1$), is considered to connect the ER PV system (converter highlighted in green). Its main functionality will be the maximum power extraction from the PV array (maximum power point (MPP) operation) or to provide any feasible reference value of power (reference power point (RPP) operation). The integration of the ER ESS is achieved by means of a half-bridge bidirectional buck–boost DC–DC converter, composed of two switches ($S_7$ and $S_8$), and one inductance ($L_{ESS}$)

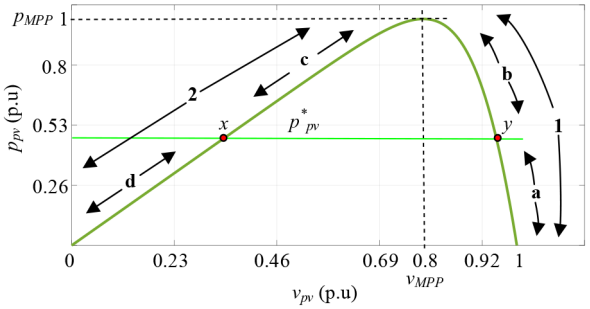


**Fig. 4** *Typical P-V curve with the different subzones for the implemented RPPT algorithm*

(converter highlighted in red). In general, this power converter will demand/inject power from/into the SC, acting as an energy buffer to meet the ER power balance. Besides, it regulates the DC bus voltage to its reference value. Finally, a three-branches two-level DC–AC power converter with the DC middle point connected to the SC electric grid neutral point is in response of the energy interaction between prosumers and the SC in terms of power trading. Moreover, this topology allows providing the SC ancillary services. Composed of six switches ($S_1$, …, $S_6$) and inductive filters ($L_a$, $L_b$ and $L_c$), this DC–AC converter (highlighted in blue colour) will be responsible for the main functionalities and services concerning active and reactive power trading, imbalance compensation and synchronisation with the SC electric grid. This converter topology can afford to include another RES, other kind of ESS, and other energy devices to fulfil the SC goals and to meet the set-points given by the SCEMS.

A 1:2 low-frequency transformer is considered before connecting the ER to the SC-PCC, in order to provide galvanic isolation, avoiding DC current injection into the SC electric grid at the same time. The use of this transformer allows the ER to operate with reduced DC-link voltage, leading to a higher protection level against indirect contacts. Other approaches such as transformerless ER or high frequency transformer-based ER can be implemented, optimising size and price. In this study, a first-order inductive grid filter ($L_i$) was used, and the internal resistance of each magnetic component ($R_{L\text{pv}}$, $R_{\text{LESS}}$ and $R_{Li}$) are considered for higher accuracy in this study. Fig. 3 also contains all the electrical variables used in subsequent sections. More details of the ER sizing and assembling are described in the following sections.

### 2.1 ER design and sizing

There are several parameters to be sized in the ER. Calculations of each passive component are summarised in this subsection.

Assuming a continuous conduction mode for the DC–DC boost converter, the minimum value of $L_{\text{pv}}$is estimated as [27]

$$L_{\text{pv}}(\text{ min }) = \frac{v_{\text{dc}}^2(v_{\text{dc}} - v_{\text{pv}})}{p_{\text{pv}}\Delta i_{\text{pv}} f_{\text{c}} v_{\text{dc}}}, \tag{1}$$

where $\Delta i_{\text{pv}}$ is the desired input current ripple in the DC–DC boost converter, and $f_{\text{c}}$ its switching frequency.

In a similar way, the calculation of the minimum value of $L_{\text{ESS}}$ can be done. In this case, the inductance value must be selected by calculating the largest value between the buck and the boost operation (1). For the buck case, the minimum value of the inductance is given by

$$L_{\text{ESS}}(\text{ min }) = \frac{v_{\text{ESS}} v_{\text{dc}}}{p_{\text{ESS}}\Delta i_{\text{ESS}} f_{\text{c}}}, \tag{2}$$

where $\Delta i_{\text{ESS}}$ is the desired input current ripple in the DC–DC buck–boost converter.

The minimum value of the DC-link capacitance ($C_{\text{dc}}$) is calculated according to [28]

$$C_{\text{dc}}(\text{ min }) = \frac{I_{C_{\text{dc}}}}{\Delta v_{\text{dc}} 2\pi f_{\text{c}}}, \tag{3}$$

with $\Delta v_{\text{dc}}$ is the desired DC-link voltage ripple, and $I_{C\text{dc}}$ is RMS DC-link capacitor current.

Finally, to estimate the minimum value of $L_i$, it was necessary to establish the harmonic component of the DC–AC converter output voltage at the switching frequency ($v_i(h_{\text{sw}})$). Considering the unity power factor, the minimum value is derived as [29]

$$L_i(\text{ min }) = \frac{V_i(h_{\text{sw}}) V_{\text{S}}}{\omega_1 h_{\text{sw}} P \,\text{THD}_I}, \tag{4}$$

where $V_{\text{s}}$is the RMS SC grid voltage and $\omega_1$ the fundamental frequency. $h_{\text{sw}}$is the switching harmonic order, $P$is the rated active power, and $\text{THD}_I$ is the total harmonic distortion of the current.

The voltage and current stresses across the components are the key parameters for dimensioning semiconductors. In the ER configuration, the voltage stress on the insulated-gate bipolar transistors (IGBTs), as well as on the diodes, is equal to the DC-link voltage, thus each semiconductor must withstand the DC-link voltage.

## 3 ER interfaces and control strategies

The SCEMS carries out a multi-criteria optimisation algorithm using as inputs: the energy price, power quality ratios (e.g., frequency deviations, RMS voltage levels and imbalance coefficients), the expected generation/demand and SoC from each prosumer's ESS, in order to manage each local ER and satisfy the SC requirements [14–21]. From this point, the SCEMS proposes and sends the operation modes, the active power and the reactive reference set-points to each ER, in order to meet them at the SC-PCC and also inside the different ER power resources and interfaces (RPPs for the PV converters and charging/discharging reference points for the ESS).

To make easier the understanding of the implemented control strategies, the reference generation and its tracking technique, the following sign convention is defined. If the active power set-point is positive ($p^* > 0$), then the ER injects active power into the SC. If the active power set-point is negative ($p^* < 0$), then the ER demands power from the SC. The same sign convention is used for the reactive power. Regarding the ESS, if the ESS set-point is positive ($p^*_{\text{ESS}} > 0$), the ESS discharges, and charges when the ESS set-point is negative ($p^*_{\text{ESS}} < 0$).

### 3.1 PV interface

One of the principal design objectives of a PV power system was to obtain the maximum power and inject it into the utility grid [30]. In order to increase the ER degree of adjustability, a RPP tracking algorithm (RPPT) was implemented based on [31]. The ER low-level controller solves the RPPT algorithm, generating the proper duty cycle ($D_{\text{pv}}$) to control the PV array working point, derived from the SCEMS. RPP operation is used instead of MPP, due to saturation limits of the ESS (surpassing its maximum voltage limit could be dangerous), and also the prevention of overvoltage in some critical periods and in certain buses during the SC electric grid operation (also known as active power curtailment technique [25]).

It is important to note that the implemented RPPT algorithm can also work at the MPP operation. The algorithm is based on the perturb and observe (P&O) method with adaptive step to maximise the performance and minimise the power fluctuations. A typical $P$–$V$ curve is shown in Fig. 4, where two different subzones ($a$ and $b$) placed at the right of the MPP (called zone 1) and another two subzones ($c$ and $d$) placed at the left of the MPP (called zone 2) are observed. Just zones 1 and 2 are distinguished for the MPP tracking, otherwise zones $a$, $b$, $c$ and $d$ must be analysed. There are two feasible PV points in the curve that match a set-point given by the SCEMS (marked as $x$ and $y$). The one located at the right side

**Table 1** Truth table to select the subsequent $D_{pv}$ in the MPPT algorithm

| $\Delta D_{pv,n}$ | $D_{pv,n}$ | $\Delta p_{pv,n}$ | $\Delta v_{pv,n}$ | $D_{pv,n+1}$ | Zone |
|---|---|---|---|---|---|
| >0 | *x* | >0 | <0 | $D_{pv,n} + \delta_{pv}$ | **1** |
| <0 | *x* | <0 | >0 | $D_{pv,n} + \delta_{pv}$ | **1** |
| >0 | *x* | <0 | <0 | $D_{pv,n} - \delta_{pv}$ | **2** |
| <0 | *x* | >0 | >0 | $D_{pv,n} - \delta_{pv}$ | **2** |

**Table 2** Truth table to select the following subsequent $D_{pv}$ in the RPPT algorithm

| $\Delta D_{pv,n}$ | $D_{pv,n}$ | $p_{pv,n} - p^*_{pv}$ | $\Delta p_{pv,n}$ | $\Delta v_{pv,n}$ | $D_{pv,n+1}$ | Subzone |
|---|---|---|---|---|---|---|
| >0 | *x* | <0 | >0 | <0 | $D_{pv,n} + \delta_{pv}$ | **a** |
| <0 | *x* | <0 | <0 | >0 | $D_{pv,n} + \delta_{pv}$ | **a** |
| >0 | *x* | >0 | >0 | <0 | $D_{pv,n} - \delta_{pv}$ | **b** |
| <0 | *x* | >0 | <0 | >0 | $D_{pv,n} - \delta_{pv}$ | **b** |
| >0 | *x* | >0 | <0 | <0 | $D_{pv,n} - \delta_{pv}$ | **c** |
| <0 | *x* | >0 | >0 | >0 | $D_{pv,n} - \delta_{pv}$ | **c** |
| >0 | *x* | <0 | <0 | <0 | $D_{pv,n} - \delta_{pv}$ | **d** |
| <0 | *x* | <0 | >0 | >0 | $D_{pv,n} - \delta_{pv}$ | **d** |

**Table 3** Logic for adaptive step reduction

| $\Delta D_{pv,n-5}$ | $\Delta D_{pv,n-4}$ | $\Delta D_{pv,n-3}$ | $\Delta D_{pv,n-2}$ | $\Delta D_{pv,n-1}$ | $\Delta D_{pv,n}$ | $\lvert\Delta D_{pv,n+1}\rvert$ |
|---|---|---|---|---|---|---|
| <0 | <0 | >0 | >0 | <0 | <0 | $k_{adp}\ x\ \lvert\delta_{pv}\rvert$ |
| >0 | <0 | <0 | >0 | >0 | <0 | $k_{adp}\ x\ \lvert\delta_{pv}\rvert$ |
| >0 | >0 | <0 | <0 | >0 | >0 | $k_{adp}\ x\ \lvert\delta_{pv}\rvert$ |
| <0 | >0 | >0 | <0 | <0 | >0 | $k_{adp}\ x\ \lvert\delta_{pv}\rvert$ |

**Table 4** Logic for adaptive step increment

| $\Delta D_{pv,n-5}$ | $\Delta D_{pv,n-4}$ | $\Delta D_{pv,n-3}$ | $\Delta D_{pv,n-2}$ | $\Delta D_{pv,n-1}$ | $\Delta D_{pv,n}$ | $\lvert\Delta D_{pv,n+1}\rvert$ |
|---|---|---|---|---|---|---|
| >0 | >0 | >0 | >0 | >0 | >0 | $1/k_{adp}\ x\ \lvert\delta_{pv}\rvert$ |
| <0 | <0 | <0 | <0 | <0 | <0 | $1/k_{adp}\ x\ \lvert\delta_{pv}\rvert$ |

of the MPP (within zone 1) is a better operation point since the PV voltage will be higher, leading to a reduced $D_{pv}$. As the DC-link voltage is regulated by the ESS DC–DC converter, the more the $D_{pv}$ rises, the further the system moves to the left side of the *P–V* curve.

The variables measured to perform the RPPT algorithm are the PV current ($i_{pv}$) and the PV voltage ($v_{pv}$) (see Fig. 3). Depending on the observed magnitudes PV power ($p_{pv}$) and $v_{pv}$ and their previous values, it is possible to determine the $D_{pv}$ to be applied, that is, to determine the new direction of the perturbation step ($\delta_{pv}$). The direction of $\Delta D_{pv}$ depends on the subzones (*a*, *b*, *c* or *d*) where the system is operating. In general, three possibilities exist:

i. $p^*_{pv} < p_{MPP}$ and $v_{pv} \geq v_{MPP}$. Desired operation subzones (*a* and *b*). The observation of the current measurements together with the previous perturbation direction and measurements will guide the system to the set-point.
ii. $p^*_{pv} < p_{MPP}$ and $v_{pv} < v_{MPP}$. Subzones (*c* and *d*) to be avoided. A negative value of $\delta_{pv}$ (system displacement to the right side of the *P–V* curve is mandatory).
iii. $p^*_{pv} \geq p_{MPP}$. The system will reach the MPP.

The implemented truth table in the low-level controller to select the subsequent $D_{pv}$ according to the aforementioned reasoning is presented in Tables 1 and 2, depending on MPP or RPP operation. Once the algorithm achieves a convergence solution and the PV system is working around the RPP or MPP, $\delta_{pv}$ is reduced to improve the steady-state performance. The adjustment of $\delta_{pv}$ is done by observing the sign of the last perturbations (in this approach, the sign of six perturbations are collected in an array, from $\Delta D_{pv,n-5}$ to $\Delta D_{pv,n}$). When the pattern of the signs is as in Table 3, the value $\delta_{pv}$ is multiplied by the adaptive factor ($k_{adp}$). This iterative process is executed until $\delta_{pv}$ gets a minimum value. Similarly, if the direction of $\delta_{pv}$ presents the same sign during six perturbations, the value of $\delta_{pv}$ is reset multiplying by $1/k_{adp}$ until obtaining the initial value. This reset (see Table 4) is considered to obtain a faster dynamic response during a change in the set-points or in partial shadows condition.

### *3.2 ESS interface*

The integration of the ESS into the local ER allows the minimisation of RES fluctuation, allowing to act as energy buffers into the SC electric grid. The effect of using any ESS is graphically explained in Fig. 5 (PV and ESS power circles). Each power converter of the ER (DC–DC and DC–AC) has extra-capacity, limited by the rated current of its semiconductor devices, that is, a maximum apparent power ($s_{MAX,i}$). This extra-capacity can be used for providing ancillary services to the SC, regulating the active and reactive power flows with strategic purposes. Moreover, ESS allows a 4-quadrant operation ER, instead of a 2-quadrant one when using only the PV system. The ESS can make the system works at point 2 (in Fig. 5) instead of 1 (if needed) or at point 4, raising the ER degree of adjustability.

The implemented strategy to generate the proper reference current ($i^*_{ESS}$) to be tracked by the half-bridge bidirectional buck–boost DC–DC converter is depicted in Fig. 6. $i^*_{ESS}$ is composed by adding two terms:

i. The main term ($i^*_{ESS\_1}$) is derived as the current needed to meet the active power balance (neglecting the losses) on the battery side and determined by the SCEMS. This term is calculated as

$$i^*_{ESS\_1} = \frac{p^*_{ESS}}{v_{ESS}}, \tag{5}$$

where $p^*_{ESS}$ and $v_{ESS}$ are the ESS reference power and the measured ESS voltage, respectively.

ii. The second term ($i^*_{ESS\_2}$) aims to control the DC-link voltage ($v_{dc}$) at the desired level ($v^*_{dc}$), as well as to compensate the power losses in the energy conversion and the small variations in the estimation of the plant parameters. This $i^*_{ESS\_2}$ is obtained from the output of the PI regulator.

Therefore, the active power balance and $p^*_{ESS}$ are accomplished at the SC-PCC, matching on the battery side as well. That is, the demanded/injected power from/to the ESS ($p_{ESS}$) will be higher or smaller than $p^*_{ESS}$, depending on the discharging or charging ESS operation, respectively.

With the goal to maintain the ESS state of health (SoH), avoiding the ESS stress as much as possible, a charging and discharging boundaries must be considered (in our case, 80% for charging and 20% for discharging). Besides, the system cannot surpass the $s_{MAX,i}$ in any power converter. In this sense, the saturation block in Fig. 6 is justified by the following:

i. The ESS must be operated within a healthy SoC margin, which depends on the ESS technology but, roughly, it can be assumed a margin between the 20 and 80% of the ESS rated capacity ($Q_{ESS}$).

Assuming that the initial value of the SoC ($SoC_0$) may be known, the real time SoC ($SoC_i$) can be estimated by the Coulomb counting method, integrating the ESS current flow over the time. In our case, the current flowing from the ESS to the DC-link is measured as positive (ESS discharging), and $SoC_i$ is expressed as

$$SoC_i(\%) = SoC_0(\%) - \frac{\int_{t_0}^{t_i} i_{ESS}(t)\,dt}{3600 Q_{ESS}} \times 100, \tag{6}$$

with $i_{ESS}$ in (A) and $Q_{ESS}$ in (Ah). Besides the saturation of $i_{ESS}$ as a function of the $SoC_i$, the ESS charging/discharging curves from manufacturer's datasheet should also be considering, limiting the maximum $i_{ESS}$ during charging or discharging, depending on the $v_{ESS}$.

ii. Once $p^*$, $q^*$, $p^*_{pv}$ are set, the SCEMS has to include a priority policy for the ER. The priority condition is based on the premise that $s_{MAX,i}$ in any power converter cannot be exceeded. Two priorities are considered active power priority and reactive power priority. If the reactive power priority is activated, $p^*_{ESS}$ must saturate its possible value to prevent ER overcurrent of the inverter

$$p^*_{ESS} \leq \sqrt{s^2_{MAX,inv} - p^2_{pv} - q^2}, \tag{7}$$

where $s_{MAX,inv}$ is the $s_{MAX,i}$ of the inverter, $p_{pv}$ is the extracted power from the PV and $q$ is the injected reactive power into the SC by the ER. The active power priority will be discussed further as it does not affect to the $p^*_{ESS}$ saturation.

At the same time, decreasing charging/discharging $i^*_{ESS}$ rates contributes to the SoH maintenance. Ramp rate control of the $v^*_{dc}$ is considered for the DC-link pre-charge process. It is important to note that the control of the DC-link voltage by the ESS allows to developed control strategies for SC operation in islanded mode.

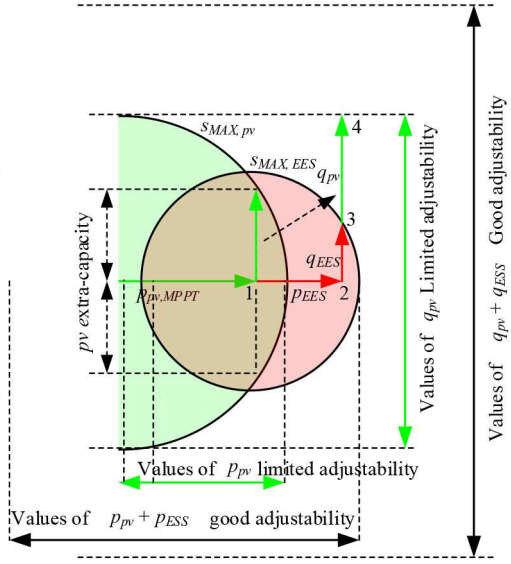


**Fig. 5** *ER power capacity representation*

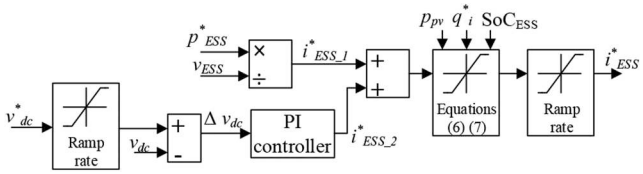


**Fig. 6** *Block diagram of the ESS control strategy*

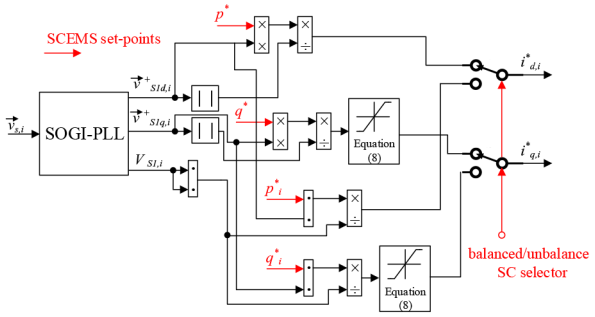


**Fig. 7** *Block diagram of the DC–AC converter*

### 3.3 Grid interface

As previously mentioned, the DC–AC converter will be responsible for the main functionalities and services concerning active and reactive power trading, imbalance compensation and synchronisation with the SC electric grid. This section explains the implemented ER control strategy, and its block diagram is depicted in Fig. 7.

*3.3.1 Active power control:* The ER accomplishes its $p^*$ by a sinusoidal source current (SCC) control strategy [32], which aims to regulate the ER in such a way that the ER injects or demands current into/from the SC-PCC, in phase with the direct components ($d$) of positive-sequence fundamental voltage. At the same time, the ER output current will have no harmonic content. By using this control strategy, in the ER2SC-P mode, the injected current is sinusoidal and in phase with the $d$ of the positive-sequence fundamental voltage. In the SC2ER-P mode, the current demanded from the SC grid is sinusoidal and against phase with the $d$ positive-sequence fundamental voltage.

The $d$ component of the ER reference currents, ($i^*_{d,i}$), is calculated as

$$i^*_{d,i} = \frac{p^*}{|v^+_{S1d,i}|} v^+_{S1d,i}, \tag{8}$$

where $\boldsymbol{v}^{+}_{s1d,i}$ is the unit vector of the direct components of the positive-sequence fundamental component of the phase-to-neutral SC grid voltage and $|\boldsymbol{v}^{+}_{s1d,i}|$ is its module. The unit vector is calculated using (9), where $v^{+}_{s1d,i}$ are the instantaneous $d$ of the positive-sequence fundamental component of the phase-to-neutral SC grid voltage

$$\boldsymbol{v}^{+}_{S1d,i} = \frac{\begin{bmatrix} v^{+}_{S1d,a} \\ v^{+}_{S1d,b} \\ v^{+}_{S1d,c} \end{bmatrix}}{\sqrt{{v^{+}_{S1d,a}}^{2} + {v^{+}_{S1d,b}}^{2} + {v^{+}_{S1d,c}}^{2}}}, \tag{9}$$

A second-order generalised integrator phase locked loop (SOGI-PLL) is employed to extract the fundamental component of the grid voltages [33].

*3.3.2 Reactive power control:* The ER is able to provide SC voltage support, improvement of the SC global power factor, motivated by economic reasons, contributing to the $CO_2$ reduced emissions (as the losses are reduced). Based on these assumptions, the SCEMS has calculated $q^*$ for each ER.

A quadrature ($q$) sinusoidal current control strategy [7], similar to the previous SCC is used for this purpose. It allows the ER to inject or demand sinusoidal current into/from the SC-PCC, in phase and in quadrature with positive-sequence fundamental voltage. Similar to the active power reference current generation, it is derived that

$$i^{*}_{q,i} = \frac{q^{*}}{|\boldsymbol{v}^{+}_{S1q,i}|}\boldsymbol{v}^{+}_{S1q,i}, \tag{10}$$

where $\boldsymbol{v}^{+}_{s1q,i}$ is the unit vector of the $q$ components of the positive-sequence fundamental component of the phase-to-neutral SC grid voltage, being +90° phase shifted from $\boldsymbol{v}^{+}_{s1d,i}$. and $|\boldsymbol{v}^{+}_{s1q,i}|$ is its module. Similarly, $\boldsymbol{v}^{+}_{s1q,i}$ is calculated as follows:

$$\boldsymbol{v}^{+}_{S1q,i} = \frac{\begin{bmatrix} v^{+}_{S1q,a} \\ v^{+}_{S1q,b} \\ v^{+}_{S1q,c} \end{bmatrix}}{\sqrt{{v^{+}_{S1q,a}}^{2} + {v^{+}_{S1q,b}}^{2} + {v^{+}_{S1q,c}}^{2}}}, \tag{11}$$

where $v^{+}_{s1q,i}$ are the instantaneous $q$ components of the positive-sequence fundamental component of the phase-to-neutral SC grid voltage.

As aforementioned, $q^*$ must be saturated if the SCEMS establishes the active power priority. In order to avoid surpassing $s_{\mathrm{MAX,inv}}$ the following restriction have to be implemented

$$q^{*} \le \sqrt{S^{2}_{\mathrm{MAX,inv}} - (p_{\mathrm{pv}} + p_{\mathrm{ESS}})^{2}}. \tag{12}$$

*3.3.3 Imbalance compensation:* A classical three-phase inverter with three-wire is used the majority of the PV installations to inject a balanced power.

However, the consumption by the SC is not balanced, causing voltage unbalanced at the SC nodes. On account of that, the ER was conceived with a three-phase four-wire topology as previously mentioned. This characteristic allows the development of phase balancing control strategies, enabling the ER to provide the compensation of load imbalance ancillary service to the SC. In this sense, the ER contributes to the SC power quality improvement in terms of voltage balancing. This control strategy only comes into operation when the SCEMS verifies any voltage unbalance in some SC nodes.

Owing to the three-branches DC–AC power converter topology with the DC middle point connected to the SC electric grid neutral point (three-phase four-wire system), independent references per phase can be generated and tracked property (ER performs as three independent single-phase systems). Both $p^*$ and $q^*$ are individually calculated by the SCEMS, establishing independent active and reactive power references per phase ($p^{*}_{i}$ and $q^{*}_{i}$). By means of this approach, (8) and (10) are redefined to (13) and (14), respectively, where $i^{*}_{d,i}$ and $i^{*}_{q,i}$ represent the $d$ and $q$ components of the per-phase reference ER current, respectively, $V_{S1,i}$ the RMS fundamental component of the phase $i$-to neutral grid voltage, and $v_{S1d,i}$ and $v_{S1q,i}$ are the instantaneous values of each $d$ and $q$ components of the phase $i$-to neutral grid voltage fundamental component, respectively

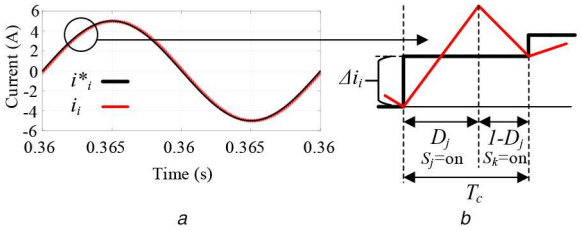


**Fig. 8** *Control diagram of the dead-beat control*
***(a)*** Reference and measured current, ***(b)*** Switching period

$$i^{*}_{d,i} = \frac{p^{*}_{i}}{V^{2}_{S1,i}} v_{S1d,i} \quad \text{and} \tag{13}$$

$$i^{*}_{q,i} = \frac{q^{*}_{i}}{V^{2}_{S1,i}} u_{S1q,i}\,. \tag{14}$$

At the same time, and similarly to the previous considerations, each $p^{*}_{i}$ and $q^{*}_{i}$ must be watched and saturated in case of surpassing $s_{\mathrm{MAX}}$ in each branch.

The ER switching signal generation for both the ESS bidirectional buck–boost DC–DC and the three-branches DC–AC power converters, with the aim of tracking their set-points given by the SCEMS, is achieved by dead-beat current controllers. This technique belongs to the family of predictive regulators, being a popular method in many recent applications, due to the low computational burden required in its implementation and calculation, and because it presents the fastest transient response and its operation at the constant switching frequency.

Figs. 8*a* and *b* illustrate the operation principle for the current tracking technique. The dead-beat algorithm calculates the necessary duty cycle to make the current reach its reference value by the end of the following modulation period. The unit delay is because of the use of the digital sampler. At any sampling time, the output of the controlled current is sampled, while the duty cycle is sent to each power converter at the same time. The consequence of this duty cycle application will be observed at the next sampling time.

$S_j$ and $D_j$ represent the top switch and its duty cycle of each converter branch, respectively ($S_1$, $S_3$, $S_5$ and $S_7$), whereas $D_k$ is the duty cycle of the bottom ones ($S_2$, $S_4$, $S_6$ and $S_8$ work in a complementary way). Assuming that $v_s$ is constant during the switching period ($T_c$) and solving the circuits presented in Fig. 3, the resulting expressions for calculating the ESS converter and the DC–AC converter duty cycles ($D_{\mathrm{ESS}}$ and $D_i$), are respectively

$$D_{\mathrm{ESS}} = \left(v_{\mathrm{ESS}} - i_{\mathrm{ESS}}R_{\mathrm{LESS}} - L_{\mathrm{ESS}}\frac{i^{*}_{\mathrm{ESS}} - i_{\mathrm{ESS}}}{T_c}\right)\frac{1}{v_{\mathrm{dc}}} \tag{15}$$

$$D_i = \left(i_i R_{Li} + Li\frac{i^{*}_{i} - i_i}{T_c} + v_{si} + \frac{v_{\mathrm{dc}}}{2}\right)\frac{1}{v_{\mathrm{dc}}} \tag{16}$$

## 4 Simulation analysis

To verify the previously described ER topology together with its control strategy as well as the main functionalities, simulations were performed using PSCAD/EMTDC, prior the real implementation, assembling and testing. It is important to note that

the required measurements are sampled to match the control frequency rate implemented in the ER controllers, making the simulation more realistic for the real implementation. The main parameters are summarised in Table 5 and will be the same used for the real ER deployment.

The ER passive elements values are calculated according to the guidelines previously described in Section 2.1. The different scenarios analysed and simulated are:

i. PV system is working at RPP, ESS discharges and charges, and the DC–AC converter injects balanced active power into the SC.
ii. PV system is working at RPP, ESS charges and the DC–AC converter injects balanced active and reactive power into the SC.
iii. PV system is working at RPP, ESS charges and the DC–AC converter injects unbalanced active and reactive power into the SC.

**Table 5** Simulation and ER parameters

| Parameter | Unit | Value |
|---|---|---|
| $v_{MPP}$ (8 panel in serial) | V | 160 |
| $P_{MPP}$ | W | 1100 |
| $v_{ESS}$ (8 lead-acid type in serial) | V | 96 |
| $Q_{ESS}$ | Ah | 7 |
| $R_{Lpv}$ | Ω | 0.1 |
| $L_{pv}$ | mH | 2.5 |
| $R_{LESS}$ | Ω | 0.25 |
| $L_{ESS}$ | mH | 2.5 |
| $R_{Li}$ | Ω | 0.1 |
| $L_i$ | mH | 5 |
| $C_1$, $C_2$ | mF | 2.2 |
| $v_{dc}^*$ | V | 500 |
| $V_{s1,i}$ (1:2 transformer) | V | 115 |
| grid frequency ($f_s$) | Hz | 50 |
| RPPT subroutine execution time ($t_{pv}$) | s | 0.2 |
| $\Delta D_{pv,0}$ | p.u. | 0.05 |
| $k_{adp}$ | p.u. | 2 |
| $K_p$ and $K_i$ (DC-link PI controller) | p.u. | 0.01 1 |
| $f_c$ | kHz | 15 |
| sampling rate | kHz | 4 |
| simulation step | µs | 0.5 |

The main long-term simulation results are displayed in Fig. 9. It encompasses each scenario previously analysed. Fig. 9*a* shows the evolution of the extracted power from the PV system, working at MPP (from 0 to 1 s, $p_{pv}$ around 1100 W) and at RPP (from 1 s until the end of the simulation, $p_{pv}$ around 800 W) at standard conditions. Fig. 9*b* represents the ESS discharge/charge cycle (180 and −180 W as ESS set-points at different times). It is possible to observe how the step response of the ESS converter is smooth, thanks to the aforementioned ramp-rate controls, contributing to maintain the ESS SoH. The resulting $p$ trading between the ER and the SC is displayed in Fig. 9*c*, where the references are fit at the SC-PCC. Finally, in Fig. 9*d*, $q$ trading is presented, with $q^*$ equal to −200 VAr (from 0.5 to 2 s) and 300 VAr (from 2.75 to 3.5 s). All the references are accurately tracked.

The first scenario studies the ER operation with the following set-points: $p_{pv}^* = 800$ W, $p_{ESS}^* = 180$ W and −180 W, $p^* = 980$ and 620 W and $q^* = 0$ VAr for each ER power stage. The references are given by the SCEMS. Fig. 10*a* shows the steady-state waveforms of $i_{pv}$, $i_{ESS}$, $v_{s,a}$ and $i_{s,a}$ as well as a detailed view of the current ripples ($\Delta_i$). The ripples are verified to be under the sizing specification (10%). Sinusoidal currents are injected into the SC with a THD less than 5%). Secondly, Fig. 10*b* depicts the same magnitudes when the ESS is being charged ($p_{ESS}^* = -180$ W and $p^* = 620$ W), with the reference values properly tracked.

Finally, the reactive power and unbalance compensation ER functionalities (scenarios 2 and 3) are analysed. Fig. 11*a* depicts the main ER waveforms at the SC-PCC, ($v_{s,a}$ and $i_{s,a}$) with the following operating references: $p_{pv}^* = 800$ W, $p_{ESS}^* = -180$ W, $p^* = 620$ W and $q^* = 0$ VAr. It is possible to observe that the injected current into the SC is completely in phase with $v_{s,a}$ (with the positive-sequence fundamental component of the phase-to-neutral SC grid voltage). Fig. 11*b*, the SCEMS has activated the reactive power control (scenario 2) in order to provide ancillary services to the SC regarding voltage issues. In this case, $q^*$ is equal to 220 VAr, which means that the ER is injecting fundamental reactive power to the SC, and $i_{s,a}$ is shifted respect to $v_{s,a}$. Fig. 11*c* shows the ER response at the PCC with the unbalance compensation strategy (scenario 3). Each phase of the DC–AC inverter receives independent set-points for both the active and the reactive power trading ($p_a^* = 114.8$ W, $p_b^* = 165$ W, $p_c^* = 248$ W, $q_a^* = 44$ VAr, $q_b^* = 59$ VAr and $q_c^* = 88$ VAr).

The transient response of the ER currents ($i_{s,i}$) is detailed in Fig. 12. $p^*$ is suddenly decreased, thus the phase currents track the new reference properly demonstrating the robustness of the current controller used.

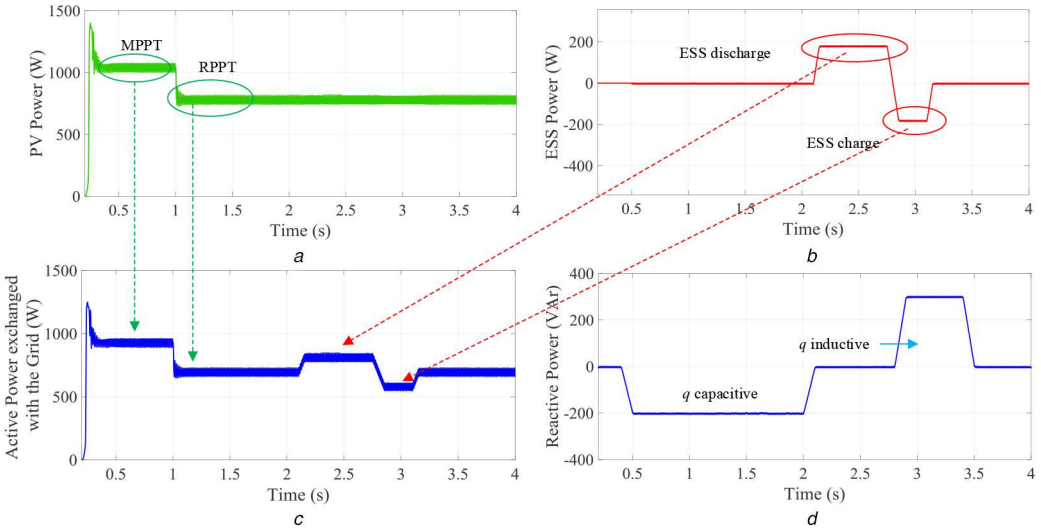


**Fig. 9** *Long-term simulation results*
***(a)*** PV power, ***(b)*** ESS power, ***(c)*** $p$ trading with the SC, ***(d)*** $q$ trading with the SC

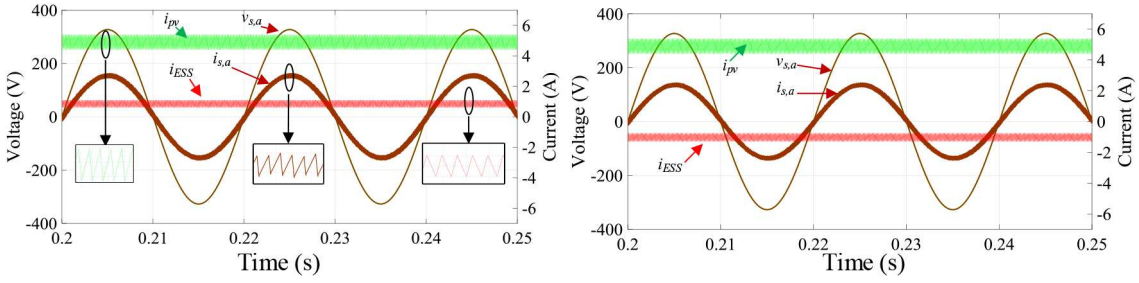


**Fig. 10** *Main ER simulated waveforms ($i_{pv}$, $i_{ESS}$, $v_{s,a}$ and $i_{s,a}$) during operation in steady state*

***(a)*** With set-points: $p^*_{pv} = 800$ W, $p^*_{ESS} = 180$ W, $p^* = 980$ W and $q^* = 0$ VAr, ***(b)*** With set-points: $p^*_{pv} = 800$ W, $p^*_{ESS} = -180$ W, $p^* = 980$ W and $q^* = 0$ VAr

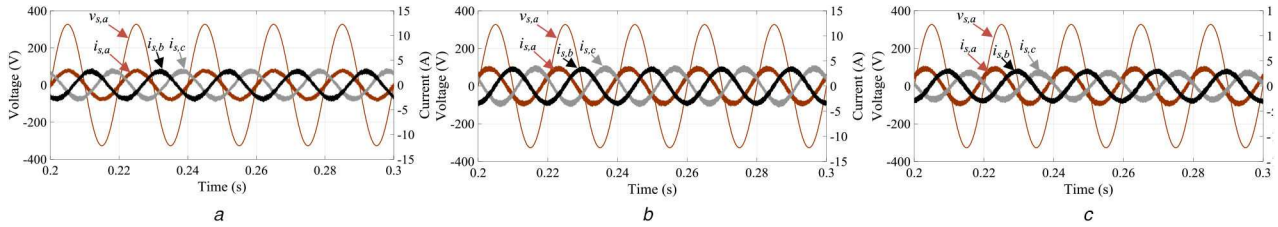


**Fig. 11** *Simulated waveforms at the SC-PCC ($v_{s,a}$ and $i_{s,i}$)*

***(a)*** Active power control, ***(b)*** Reactive power control, ***(c)*** Unbalance compensation control

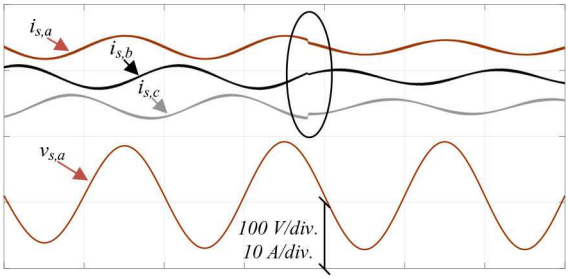


**Fig. 12** *Simulated transient response of $i_{s,i}$*

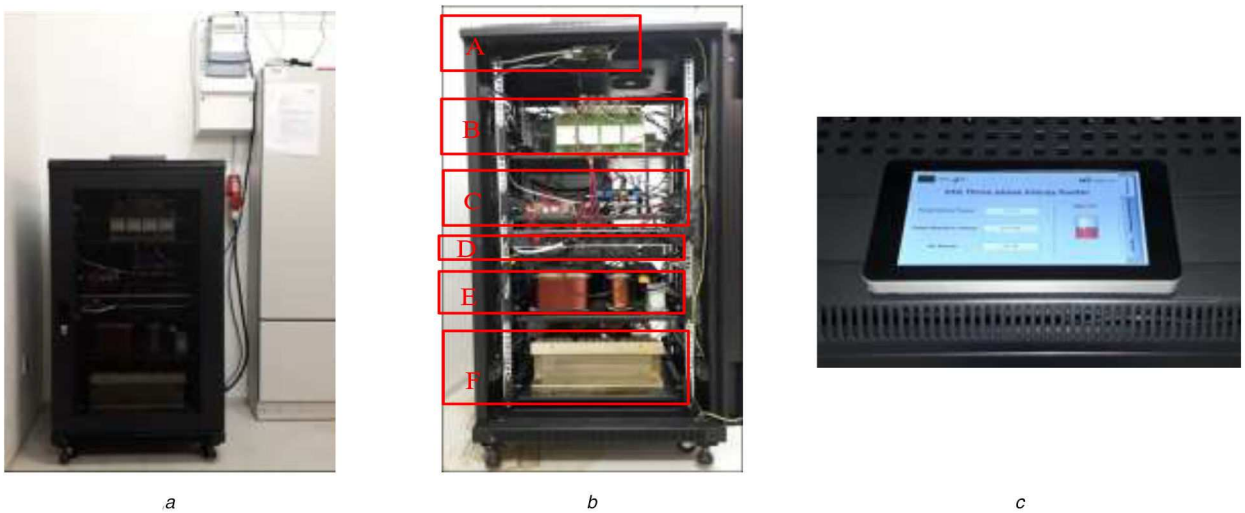


**Fig. 13** *ER prototype*

***(a)*** ER deployed, ***(b)*** ER cabinet front view (from top to bottom): high-level controller as SCEMS (box A), power electronic converters, drivers and power cables (box B), measurement and control board (box C), ESS (box D), inductive filters (box E) and isolation transformer (box F), ***(c)*** ER GUI for local control and monitoring

## 5 Experimental results

An experimental prototype of the specified ER has been assembled, tested and deployed into an SC. One of the premises was to develop the ER as a prosumer friendly equipment. Hence, the ER was installed inside a cabinet, as a 'black-box' that includes all the interfaces (see Fig. 13*a*). At the same time, the PCBs and components were assembled with a high level of modularity, to facilitate the maintenance and to be able to include another RES or ESS. In Fig. 13*b* from top to bottom: high-level controller as SCEMS (box A), power electronic converters, drivers and power cables (box B), measurement and control board (box C), ESS (box D), inductive filters (box E) and isolation transformer (box F).

The SCEMS was deployed on a Raspberry Pi 3 model B+ with a 64-bit quad-core processor running at 1.4 GHz, and dual-band 2.4 and 5 GHz wireless LAN with modular compliance certification. These characteristics enable the SCEMS (high-level controller) to run complex algorithms, to receive data from the devices

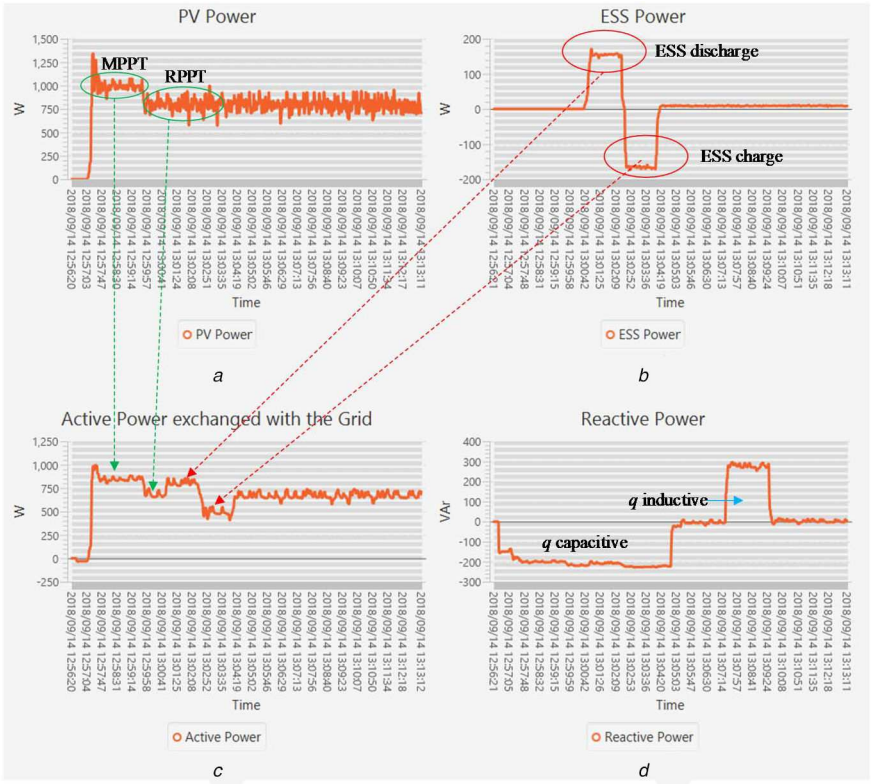


**Fig. 14** *Long-term experimental results*
***(a)*** PV power, ***(b)*** ESS power, ***(c)*** $p$ trading with the SC, ***(d)*** $q$ trading with the SC

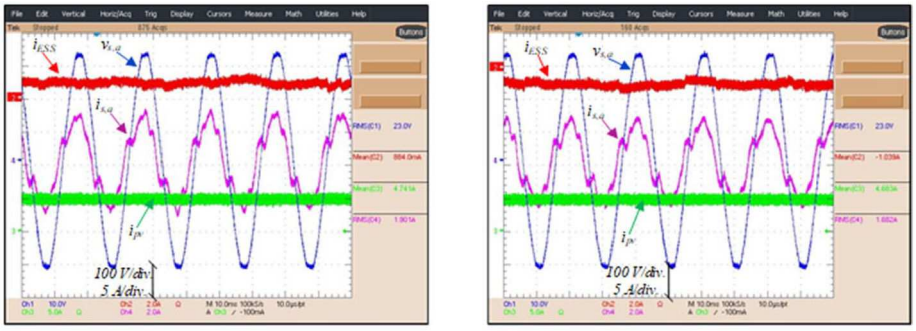


**Fig. 15** *Main ER experimental waveforms ($i_{pv}$, $i_{ESS}$, $v_{s,a}$ and $i_{s,a}$) during operation in steady state*
***(a)*** With set-points: $p^*_{pv} = 800$ W, $p^*_{ESS} = 180$ W $p^* = 980$ W and $q^* = 0$ VAr, ***(b)*** With set-points: $p^*_{pv} = 800$ W, $p^*_{ESS} = -180$ W $p^* = 620$ W and $q^* = 0$ VAr

connected to the SC and to send to the different ER set-points. The IGBTs selected for the power electronic converters were the SEMIKRON SKM50GB12T4 branch module, driven by the SKYPER 32 driver. The measurement stage has been implemented by Hall effect transducers, with galvanic isolation, LA 55P/SP1 for measuring DC and AC currents and LV 25-P for measuring DC and AC voltages, both by LEM. These sensors work with high precision, good linearity and low common mode disturbance. The low-level control system is based on the Arduino Due board. This board is based on the Atmel SAM3X8E ARM Cortex-M3 CPU (32-bit ARM core microcontroller), able to operate at a maximum frequency of 84 MHz. At the same time, this Arduino includes the required analogue inputs and PWM output channels to control the developed ER. This board was also extended with the required auxiliary circuits to make it fully compatible with the measurement and driver systems. The different control strategies explained in Section 3 were implemented on it, in order to generate the different switching signals. Finally, Fig. 13*c* shows the ER graphical user interface (GUI) which enables the prosumer's control and monitoring.

The same scenarios than in simulation were used for the experimental for a better comparison and validation of the results. It was used PV panels and the ESS described in Table 5. Fig. 14 shows the experimental long-term results, collected by the SCEMS. First, Fig. 14*a* shows the extracted power from the PV system, working first at MPP, and then at RPP (with $p^*_{pv}$ around 800 W). Fig. 14*b* represents an ESS discharge/charge cycle (180 and −180 W) with a smooth step response. The resulting $p$ trading between the ER and the SC is displayed in Fig. 14*c*, fitting the references at the SC-PCC. Lastly, in Fig. 14*d*, $q$ trading is displayed, with $q^*$ equal to −200 and 300 VAr.

Scenario 1 aims to experimentally validate the ER operation in steady conditions with the set-points $p^*_{pv} = 800$ W, $p^*_{ESS} = 180$ W and −180 W, $p^* = 980$ and 620 W and $q^* = 0$ VAr. Figs. 15*a* and *b* show the waveforms of $i_{pv}$, $i_{ESS}$, $v_{s,a}$ and $i_{s,a}$ both in the ESS discharge and charge. Reference values were properly tracked in both cases. It is important to note that the distortion presented in $i_{s,a}$ is explained by the open-circuit current demanded by the 1:2 isolation transformer connected between the ER and the SC. Current probes were placed during these measurements in the secondary side (SC side), affecting the injected current. Nerveless, it was verified that the THD was less than 7%. Fig. 16 shows the active, reactive, and unbalance control. Fig. 16*a* depicts the real ER waveforms at the SC-PCC, ($v_{s,a}$ and $i_{s,a}$) with the same simulated operating set-point: $p^*_{pv} = 800$ W, $p^*_{ESS} = -180$ W, $p^* = 620$ W

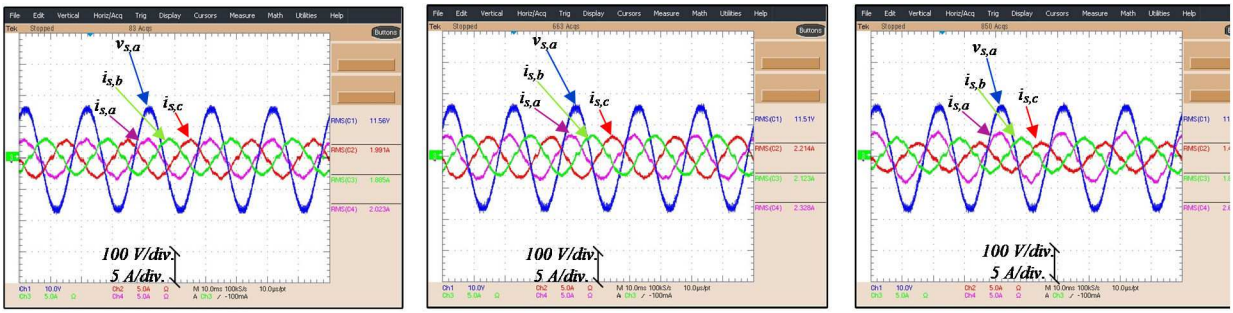


**Fig. 16** *Experimental waveforms at the SC-PCC ($v_{s,a}$ and $i_{s,i}$)*
***(a)*** Active power control, ***(b)*** Reactive power control, ***(c)*** Unbalance compensation control

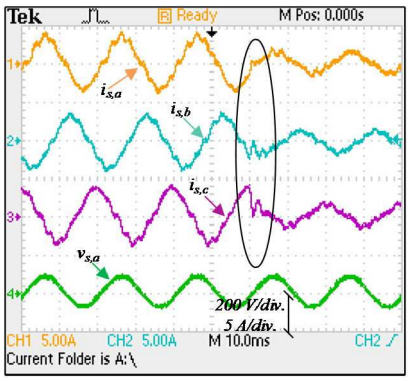


**Fig. 17** *Experimental transient response of $i_{s,i}$*

and $q^*=0$ VAr. ER operation with the reactive power control is observed in Fig. 16*b* ($q^*$ is equal to 220 VAr, where $i_{s,a}$ is shifted respect to $v_{s,a}$. Fig. 16*c*shows the ER operation with the unbalance compensation strategy ($p_a^* = 114.8$ W, $p_b^* = 165$ W, $p_c^* = 248$ W, $q_a^* = 44$ VAr, $q_b^* = 59$ VAr and $q_c^* = 88$ VAr). Finally, the transient response of $i_i$ is depicted in Fig. 17 under a step $p^*$ change. Figs. 16 and 17 show the injected current by the ER. In these cases, the current probes are placed in the ER side, thus, open-circuit current demanded by the transformer does not appear.

## 6 Conclusions

Control strategies for a local ER within an SC regarding active and reactive power flow control have been implemented and successfully validated. Additionally, a control strategy to compensate the possible voltage imbalance in some SC electrical grid nodes is also presented. The distribution of the active power interchange between the small-scale RES and the small-scale ESS is considered to increase the controllability of the ER, maintaining the SoH of the ESS. The simulation and experimental verification show the correct operation of the ER, tracking the set-points provided by the SCEMS with accuracy and quality. These results demonstrate that the ER with a proper control strategy can provide ancillary services to the SC, and increase the SC stakeholder benefits as bill saving, power factor improvement and imbalance compensation.

## 7 Acknowledgment

The research work leading to these results has received funding from the Portuguese National Funds through FCT – Fundação para a Ciência e a Tecnologia in the context of the UID/EEA/00066/2019 project and from the European Union's Horizon 2020 research and innovation programme under grant agreement No 731155 – Storage4Grid project. The sole responsibility of this publication lies with the authors. The European Union is not responsible for any use that may be made of the information contained therein. The authors also acknowledge to the Junta de Extremadura (Regional Government) within the program "Ayudas Talento" (TA18003) the co-support for this work.

## 8 References

[1] National Institute of Standards and Technology (NIST): 'NIST framework and roadmap for smart grid interoperability standards', 2014, Release 3.0
[2] Eissa, M.M.: 'Challenges and novel solution for wide-area protection due to renewable sources integration into smart grid: an extensive review', *IET Renew. Power Gener.*, 2018, **12**, (16), pp. 1843–1853
[3] Jiang, W., Zhang, L., Zhao, H., *et al.*: 'Research on power sharing strategy of hybrid energy storage system in photovoltaic power station based on multi-objective optimisation', *IET Renew. Power Gener.*, 2016, **10**, (5), pp. 575–583
[4] Guerrero-Martinez, M.A., Milanés-Montero, M.I., Barrero-González, F., *et al.*: 'A smart power electronic multiconverter for the residential sector', *Sensors*, 2017, **17**, (6), p. 1217
[5] Miñambres-Marcos, V.M., Guerrero-Martinez, M.A., Barrero-González, F, *et al.*: 'A grid connected photovoltaic inverter with battery-supercapacitor hybrid energy storage', *Sensors*, 2017, **17**, (8), p. 1856
[6] Qiu, J., Zhao, X., Zheng, Y., *et al.*: 'Distributed generation and energy storage system planning for a distribution system operator', *IET Renew. Power Gener.*, 2018, **12**, (12), pp. 1345–1353
[7] Milanés-Montero, M.I., Barrero-González, F., Pando-Acedo, J., *et al.*: 'Smart community electric energy micro-storage systems with active functions', *IEEE Trans. Power Appl.*, 2018, **54**, (3), pp. 1975–1982
[8] Huimiao, C., Zechun, H., Hongcai, Z., *et al.*: 'Coordinated charging and discharging strategies for plug-in electric bus fast charging station with energy storage system', *IET Gener. Transm. Distrib.*, 2018, **12**, (9), pp. 2019–2028
[9] Fazeli, A., Summer, M., Christopher, E., *et al.*: 'Power flow control for power and voltage management in future smart energy communities'. 3rd Renewable Power Generation Conf. (RPG 2014), Naples, Italy, September 2014, pp. 1–6
[10] Liu, Y., Hu, S.: 'Renewable energy pricing driven scheduling in distributed smart community systems', *IEEE Trans. Parallel Distrib. Syst.*, 2017, **28**, (5), pp. 1445–1456
[11] Gungor, V.C., Sahin, D., Taskin, K., *et al.*: 'Smart grid technologies: communication technologies and standards', *IEEE Trans. Ind. Inf.*, 2011, **7**, (4), pp. 529–539
[12] Jianing, L., Zhi, W., Suyang, Z., *et al.*: 'Aggregator service for PV and battery energy storage systems of residential building', *CSEE J. Power Energy Syst.*, 2015, **1**, (4), pp. 3–11
[13] Kanchev, H., Di, L., Colas, F., *et al.*: 'Energy management and operational planning of a microgrid with a PV-based active generator for smart grid applications', *IEEE Trans. Ind. Electron.*, 2011, **58**, (10), pp. 4583–4592
[14] Ruiz-Cortés, M., González-Romera, E., Amaral-Lopes, R., *et al.*: 'Optimal charge/discharge scheduling of batteries in microgrids of prosumers', *IEEE Trans. Energy Convers.*, 2019, **34**, (1), pp. 468–477
[15] Paudel, A., Chaudhari, K., Long, C., *et al.*: 'Peer-to-peer energy trading in a prosumer-based community microgrid: a game-theoretic model', *IEEE Trans. Ind. Electron.*, 2019, **66**, (8), pp. 6087–6097
[16] Liu, N., Yu, X., Wang, C., *et al.*: 'Energy-sharing model with price-based demand response for microgrids of peer-to-peer prosumers', *IEEE Trans. Power Syst.*, 2017, **32**, (5), pp. 3569–3583
[17] Vergados, D.J., Mamounakis, I., Makris, P., *et al.*: 'Prosumer clustering into virtual microgrids for cost reduction in renewable energy trading markets', *Sustain. Energy Grids Netw.*, 2016, **7**, pp. 90–103
[18] Mengelkamp, E., Garttner, J., Rock, K., *et al.*: 'Designing microgrid energy markets: a case study: the Brooklyn Microgrid', *Appl. Energy*, 2018, **210**, pp. 870–880
[19] Carli, R., Dotoli, M., Pellegrino, R.: 'A hierarchical decision-making strategy for the energy management of smart cities', *IEEE Trans. Autom. Sci. Eng.*, 2017, **14**, (2), pp. 505–523
[20] Su, Z., Wang, Y., Xu, Q., *et al.*: 'A secure charging scheme for electric vehicles with smart communities in energy blockchain', *IEEE Internet Things J.*, 2019, **6**, (3), pp. 4601–4613
[21] Bui, V., Hussain, A., Kim, H.: 'A multiagent-based hierarchical energy management strategy for multi-microgrids considering adjustable power and demand response', *IEEE Trans. Smart Grid*, 2018, **9**, (2), pp. 1323–1333
[22] Roasto, I., Husev, O., Najafzadeh, M., *et al.*: 'Voltage source operation of the energy-router based on model predictive control', *Energies*, 2019, **12**, (10), pp. 1–15

[23] Liu, B., Wu, W., Zhou, C., *et al.*: 'An AC-DC hybrid multi-port energy router with coordinated control and energy management strategies'. *IEEE Access*, 2019, **7**, pp. 109069–109082
[24] Ren, L., Zhang, C., Du, M.: 'Power router based on conventional three-phase bridge inverter and DC-DC converter', *CIRED-Open Access Proc. J.*, 2017, **1**, pp. 391–394
[25] Yongheng, Y., Blaabjerg, F., Wang, H., *et al.*: 'Power control flexibilities for grid-connected multi-functional photovoltaic inverters', *IET Renew. Power Gener.*, 2016, **10**, (4), pp. 504–513
[26] Pires, V.F., Martins, J.F., Roncero-Clemente, C., *et al.*: 'Controlling a battery energy storage system to support residential photovoltaic installations'. 2017 IEEE 26th Int. Symp. on Industrial Electronics (ISIE) 2017, Edinburgh, UK, 2017, pp. 1–6
[27] Panfilov, D., Husev, O., Blaabjerg, F., *et al.*: 'Comparison of three-phase three-level voltage source inverter with intermediate DC–DC boost converter and quasi-Z-source inverter', *IET Power Electron.*, 2016, **9**, (6), pp. 1238–1248
[28] Mnati, M.J., Abed, J.K., Bozalakov, D.V., *et al.*: 'Analytical and calculation DC-link capacitor of a three-phase grid-tied photovoltaic inverter'. 2018 IEEE 12th Int. Conf. on Compatibility, Power Electronics and Power Engineering. (CPE-POWERENG 2018), Doha, Qatar, 2018, pp. 1–6
[29] Husev, O., Chub, A., Romero-Cadaval, E., *et al.*: 'Voltage distortion approach for output filter design for off-grid and grid-connected PWM inverters', *J. Power Electron.*, 2015, **15**, (1), pp. 278–287
[30] Romero-Cadaval, E., Spagnoulo, G., García-Franquelo, L., *et al.*: 'Grid-connected photovoltaic generation plants: components and operation', *IEEE Ind. Electron. Mag.*, 2013, **7**, (3), pp. 6–20
[31] Miñambres-Marcos, V., Guerrero-Martinez, M.A., Romero-Cadaval, E., *et al.*: 'Grid-connected photovoltaic power plants for helping node voltage regulation', *IET Renew. Power Gener.*, 2014, **9**, (3), pp. 236–244
[32] Gallardo-Lozano, J., Milanés-Montero, M.I., Guerrero-Martinez, M.A., *et al.*: 'Electric vehicle battery charger for smart grids', *Electr. Power Syst. Res.*, 2012, **90**, pp. 18–29
[33] Blaabjerg, F., Teodorescu, R., Liserre, M., *et al.*: 'Overview of control and grid synchronization for distributed power generation systems', *IEEE Trans. Ind. Electron.*, 2006, **53**, (5), pp. 1398–1409